Simulation of massively separated flows and rotating machine flows using hybrid models

Florian Miralles, Bastien Sauvage, Alexey Duben, Vladimir Bobkov, Tatiana Kozubskaya, Stephen Wornom, Bruno Koobus, Alain Dervieux

The 8th European Congress on Computational Methods in Applied Sciences and Engineering
ECCOMAS Congress 2022
5-9 June 2022, Oslo, Norway

SIMULATION OF MASSIVELY SEPARATED FLOWS AND ROTATING MACHINE FLOWS USING HYBRID MODELS ECCOMAS CONGRESS 2022

F. MIRALLES[1,*], B. SAUVAGE[2], A. DUBEN[3], V. BOBKOV[4], T. KOZUBSKAYA[5], S.F. WORNOM[6], B. KOOBUS[7], A. DERVIEUX[8]

[1,*]IMAG, Univ. Montpellier, CNRS, Place Eugène Bataillon, 34090 Montpellier, France.
florian.miralles@umontpellier.fr

[1]Univ. Côte d'Azur/INRIA Projet Ecuador, Sophia-Antipolis, France.
Bastien.Sauvage@inria.fr

[1]CAALAB, Keldysh Institute of Applied Mathematics, 4, Miusskaya Sq., Moscow, 125047, Moscow, alexey.duben@gmail.com

[1]CAALAB, Keldysh Institute of Applied Mathematics, 4, Miusskaya Sq., Moscow, 125047, Moscow, veld13@gmail.com

[1]CAALAB, Keldysh Institute of Applied Mathematics, 4, Miusskaya Sq., Moscow, 125047, Moscow, tatiana.kozubskaya@gmail.com

[1]IMAG, Univ. Montpellier, CNRS, Montpellier, France, stephen.wornom@inria.fr

[1]IMAG, Univ. Montpellier, CNRS, Montpellier, France, bruno.koobus@umontpellier.fr

[1]Lemma, Biot, France, and Univ. Côte d'Azur/INRIA Projet Ecuador, Sophia-Antipolis, France, alain.dervieux@inria.fr

Key words: Hybrid turbulence models, airfoil, rotating machine, low dissipation schemes.

Abstract. RANS, DES, hybrid RANS/DVMS and DDES/DVMS models are introduced in low dissipation schemes. They are compared for the simulation of vortex shedding flows around a NACA0021 at high angle of attack and a Caradonna-Tung helix.

1 INTRODUCTION

The overflight of cities by passenger drones and helicopters could expand once many technological issues, including noise, are resolved. For this, numerical simulation is called upon to play a major role. This paper focuses on the study of DDES and hybrid RANS-LES models for vortex shedding flows around airfoil and blades. Numerical ingredients that we study are superconvergent finite-volume schemes, devices for taking into account rotation, and mesh adaptation. Numerical experiments focus on the 3D calculation of an airfoil with large angle of attack and the rotating helix case of Caradonna and Tung. This work is done in a bilateral ANR/RSF

Franco-Russian project (ANR Project Number: ANR-19-CE40-0020-01, RSF Project Number: 20-41-09018).

2 LOW DISSIPATION SCHEMES FOR UNSTRUCTURED MESH

2.1 MUSCL and molecule extensions

The numerical approach selected in this work is basically a second-order accurate vertex centered approximation on tetrahedrizations or mixed tetra/penta/hexa meshes. Dual cells are limited by facets, which are triangles, each of them being formed by a mid-edge, a centroid of face, a centroid of an element.The assemby of fluxes is edge based. For each edge ij of the mesh, fluxes are computed through the union of facets being the common boundary between two dual cells around the vertices i and j. The flux between each couple (i,j) of cells is numerically integrated through a unique approximate Riemann solver ARS(W_{ij}, W_{ji}, ν_{ij}), in practice the Roe scheme. The integration values W_{ij} W_{ji} are two special *upwind and downwind reconstructions* of the unknown field W located at the middle I_{ij} of the edge ij. For these reconstructions, we consider two methods, each of them resulting in a superconvergent approximation. By superconvergence we mean that for some Cartesian meshes, the accuracy may be much higher than the second-order one. The purpose is not higher-order convergence in this particular context but a strong reduction of dissipation and some reduction of the dispersion in the general case of a non-Cartesian but not so irregular mesh as generated for our aeroacoustic calculations. Two low-dissipation reconstruction methods are used in this paper.

- The V6 scheme has been introduced in [6, 4]. The interpolation W_{ij} uses the value of the field and its gradient on vertex j and on the vertices of the upwind tetrahedron T_{ij}. The interpolation W_{ji} uses the value of the field and its gradient on vertex i and on the vertices of the downwind tetrahedron T_{ji}. In the AIRONUM code, the scheme is fifth-order accurate on certain Cartesian meshes, and is (solely) stabilized by a sixth-order dissipation the strength of which can be tuned by a parameter $\gamma \in]0, 1]$ (see [6, 4] for details). In the NICEFLOW code, the transient fixed point mesh adaptor of [2] can be applied, some preliminary computations will be shown.
- With the EBR scheme used in the NOISETTE code, an increase in the spatial approximation accuracy is achieved by means of the application of the quasi-one-dimensional edge-oriented reconstruction of variables from field values at a certain number of points at which line ij intersects element faces in both directions ij and ji. According to the number of intersections used, the resulting scheme is of arbitrary truncation order on Cartesian meshes made of aligned vertices. The EBR scheme is described in detail in [1, 3].

In both cases, the spatial approximation of the viscous terms is implemented using the Galerkin finite-element method based on the linear basis functions. The time integration is performed using a three-point backward Euler method of second order approximation with Newtonian linearization of the system of difference equations.

3 RANS-LES MODELS

3.1 RANS modelling

First, we want to specify that RANS stands for unsteady RANS throughout the document. In this work, and as far as the closure of the RANS equations is concerned, three low Reynolds

RANS models are used, namely the Spalart-Allmaras (SA) model [11], the $k-\varepsilon$ model proposed in Goldberg et al. [8] (KEG) and the $k-R$ model (KR) recently introduced in [14] by Zhang et al. These models were chosen, especially the last two mentioned, because of their abilities to correctly predict separated flows with adverse pressure gradients that interest us in this study. SA is the standard basis of DES and DDES models. KEG was designed to improve the predictions of the standard $k-\varepsilon$ one for adverse pressure gradient flows, including separated flows. For the sake of brevity, the equations of these two models are not recalled in this document. KR was designed with the aim of correctly capturing non-equilibrium flows with separation and adverse pressure gradient. This recent two-equations RANS model is defined by the following transport equations on k and $R = k^2/\varepsilon$:

$$\begin{aligned}
\frac{\partial \rho k}{\partial t} + \nabla\cdot(\rho \mathbf{u} k) &= \mu_t \tilde{S}^2 + \nabla\cdot\left[\left(\mu + \frac{\mu_t}{\sigma_k}\right)\nabla k\right] - \rho\frac{k^2}{R}, \\
\frac{\partial \rho R}{\partial t} + \nabla\cdot(\rho \mathbf{u} R) &= c_1 T_t \mu_t \tilde{S}^2 - \min\left(\rho c_2 k, \mu_t \frac{v}{a_1}\right) + \nabla\cdot\left[\left(\mu + \frac{\mu_t}{\sigma_\varepsilon}\right)\nabla R\right] \\
&+ \left(\mu + \frac{\mu_t}{\sigma_\varepsilon}\right)\frac{4}{k}\nabla k\cdot\nabla R - \left(f_d\,\mu + \frac{\mu_t}{\sigma_\varepsilon}\right)\frac{2R}{k^2}\|\nabla k\|_2^2 - \left(\mu + \frac{\mu_t}{\sigma_\varepsilon}\right)\frac{2}{R}\|\nabla R\|_2^2.
\end{aligned} \tag{1}$$

where $\tilde{S}$ denotes a modified mean strain-rate (see [14] for its expression) and μ_t is the turbulent viscosity defined by

$$\mu_t = \rho c_\mu f_\mu \Big[\underbrace{k T_t (1-f_c)}_{\mu_t^{(1)}} + \underbrace{R f_c}_{\mu_t^{(2)}}\Big] \tag{2}$$

in which c_μ, f_μ and T_t are given in [14], and f_c is an hybridization function defined by $f_c = \tanh\left(\max\left(0, \frac{s}{v} - 1\right)\right)$ with $s = \sqrt{2\sigma : \sigma}$ and $v = \sqrt{2\Omega : \Omega}$, σ being the strain tensor and Ω the vorticity tensor. It is worth noting that f_c is a function which tends to zero in the rotational region and unity in the irrotational region, switching between $\mu_t^{(1)}$ and $\mu_t^{(2)}$ in expression (2), $\mu_t^{(2)}$ being more suitable in shear regions.

3.2 DDES

The DDES approach allows to delay an early transition from RANS to LES in the boundary layer by modifying the length scale d of the DES model. For this purpose, an adimensionalized fonction f_{ddes}, called the delaying function, is introduced:

$$f_{\text{ddes}} = 1 - \tanh((8 r_d)^3) \quad \text{with} \quad r_d = \frac{\nu_t + \nu}{\max(\sqrt{u_{i,j}u_{i,j}}, 10^{-10}) K^2 d_w^2}.$$

where K denotes the von Kàrmàn constant ($K = 0.41$), d_w is the normal distance to the wall, $u_{i,j}$ is the derivative according to x_j of the component i of the velocity u (ν_t and ν are the turbulent kinematic viscosity and the fluid kinematic viscosity, respectively). For the DDES/Spalart-Allmaras version (DDES-SA), the length scale is then redefined as follows:

$$\tilde{d} = d - f_{\text{ddes}}\ \max(0, d - C_{DES}\Delta) \quad ; \quad C_{DES} = 0.65$$

and introduced in the closure equation:

$$\frac{D\tilde{\nu}}{Dt} = C_{b1}\tilde{S}\tilde{\nu} - c_{w1} f_w \left(\frac{\tilde{\nu}}{\tilde{d}}\right)^2 + \frac{1}{\sigma}\Big[\nabla\cdot[(\nu + \tilde{\nu})\nabla\tilde{\nu}] + c_{b2}\nabla\tilde{\nu}\cdot\nabla\tilde{\nu}\Big].$$

The DDES/two-equation models are obtained by replacing, in the ρk transport equation, the dissipation term by a DDES dissipation introducing the characteristic length l_{ddes}:

$$\frac{\partial \rho k}{\partial t} + \frac{\partial (\rho \widetilde{v_j} k)}{\partial x_j} = \frac{\partial \left[\left(\mu + \frac{\mu_t}{\sigma_k} \right) \frac{\partial k}{\partial x_j} \right]}{\partial x_j} + \tau_{ij} \frac{\partial v_i}{\partial x_j} - \rho \frac{k^{3/2}}{l_{\text{ddes}}}$$

$$\text{where} \quad l_{\text{ddes}} = \frac{k^{3/2}}{\varepsilon} - f_{\text{ddes}} \ \max(0, \frac{k^{3/2}}{\varepsilon} - C_{DES}\Delta)$$

and for the $k - R$ model, $\varepsilon = k^2/R$.

3.3 Hybridation with DVMS

3.3.1 DVMS

Several LES models behave in most cases better than a baseline Smagorinsky model, while still being very simple (no extra equation). Among them, the dynamic subgrid-scale (DSGS) model and the variational multiscale approach (VMS) which is aimed at limiting the effects of the SGS closure model to the smallest resolved scales. In [10] we define DVMS, a combination of both models which is not computer intensive and, at the same time, produces better prediction for the test cases we tried. In the computations performed in this work, the SGS model is that of Smagorinsky.

3.3.2 Hybridation

Our hybrid strategies are based on a blending of either the RANS or DDES model with the DVMS approach. After semi-discretization, the hybrid equations can be written as:

$$\left(\frac{\partial W_h}{\partial t}, \Phi_i \right) + (\nabla \cdot F(W_h), \Phi_i) = -\theta \left(\tau^{mod}(W_h), \Phi_i \right) - (1 - \theta) \left(\tau^{DVMS}(W_h'), \Phi_i' \right)$$

where the stress tensor τ^{mod} is defined by first choosing one of the three above RANS model, then τ^{mod} holds for either the RANS stress tensor or the stress tensor for a DDES model built with the chosen RANS approach. τ^{DVMS} is the SGS term that applies in DVMS on the small resolved components W_h' of the hybrid variable W_h, Φ_i denotes the basis and test functions, F denotes the convective and viscous fluxes, and θ is the blending function.
The blending function plays a key role in our hybrid models since, according on its value, the model behaves like a RANS (or DDES) model, like a DVMS model, or between these two modes. This function must be able to allow an automatic and progressive switch from RANS to DVMS where the grid resolution is fine enough to resolve a significant part of the local turbulence scales or fluctuations, i.e. computational regions suitable for DVMS computations. Additionally, this blending function should prevent the activation of the DVMS model in the boundary layer, which would otherwise require a too fine mesh in order to obtain a good prediction of this region of the flow. Typically, it is desirable to use the RANS (or DDES) model around the body and the DVMS model elsewhere (if the fineness of the mesh allows it), in particular in the wake in order to more accurately predict the propagation of the fluctuations of the flow like those of pressure in the case of an aeroacoustic calculation. Indeed, the low dissipation introduced by the DVMS approach reduces the damping of such turbulent structures.

In this work, two blending functions are applied which can write as $\theta = 1 - f_d(1-\tanh(\xi^2))$ with $\xi = \frac{\Delta}{l_{RANS}}$ where l_{RANS} denotes the characteristic RANS scale ($l_{RANS} = \frac{k^{3/2}}{\varepsilon}$), Δ is the filter width (defined in this study as the cubic root of the grid element volume), and f_d is a shielding function characterizing each of the two blending functions:

- *Option 1*: $f_d = f_{\text{ddes}}$ the delaying function used in DDES (see Section 3.2)

- *Option 2*: $f_d = f_{\text{geo}} = \exp\left(-\frac{1}{\epsilon}\min^2(d-\delta_0, 0)\right)$ with d the normal distance to the wall, $\epsilon > 0$ small enough and $\delta_0 > 0$ (of the order of the boundary layer thickness).

For illustration, isocontours of the blending function with *Option 1* and *Option 2* are given in Fig. 1 (left and right, respectively) for the flow past a NACA0021 at 60° angle of attack. In particular, it can be noted that the RANS model is activated in the boundary layer ($\theta \to 1$) whereas the VMS component is activated in the wake ($\theta \to 0$). It can also be observed that the use of the shielding function $f_d = f_{\text{geo}}$ results in a narrower region around the body in which the RANS model is activated.

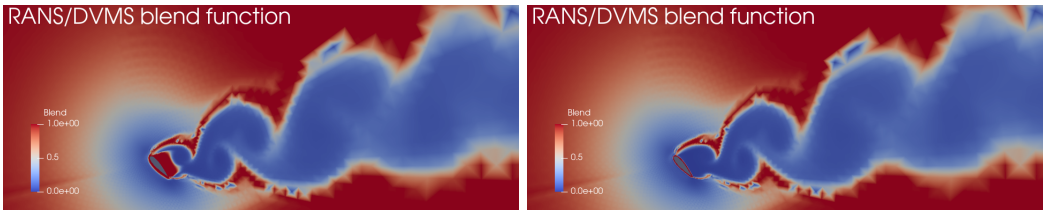

Figure 1: Blending function isocontours with *Option 1* (left) and *Option 2* (right) for the NACA0021 benchmark at 60° angle of attack (Reynolds 10^6): for $\boldsymbol{\theta = 1}$ (in red) the RANS component is activated, and in the limit $\boldsymbol{\theta \to 0}$ (in blue) DVMS is restored.

4 FLOW PAST A NACA0021

This first application concerns the flow around a NACA0021 airfoil in a deep stall which is characterized by massive separations. The angle of attack is set to 60°. The free stream Mach number and the ambient turbulence intensity are respectively M=0.1 and $Tu = 0.6\%$. Chord-based (c= 0.125[m]) Reynolds number is $Re_c = \rho U_0 c/\mu = 2.7.10^5$. Experimental investigations are published in [12, 13]. A 3D fixed mesh of 0.5M vertices has been used with AIRONUM software. It is made of 33 slices, each of them being an O-type structured grid with 101 nodes in the azimuthal direction and 140 in the radial direction (the first vertex row is at $y^+ = 0.7$). The computational domain is such that $-15 < x, y < 15$, and $0 < z < Lz = 1c$, where x, y, z denote the streamwise, transverse and spanwise directions respectively. Periodic boundary conditions are set for the spanwise direction. Beside, a mesh adapted calculation with 0.2M vertices has been performed with NiceFlow code.
For the purpose of comparison, the Russian team of our collaborative ANR/RSF project carried out calculations with the NOISette software on three 3D meshes which are more refined in the

azimuthal direction compared to the fixed mesh mentioned above. The O-type structured grid, constituting each slice of these 3D meshes, contains 211 nodes in the azimuthal direction and 140 in the radial direction (the first vertex row is at $y^+ = 0.7$). The first mesh (1.15M nodes), called Mesh1 in this section, is made of 33 slices in the transverse direction with a wingspan $Lz = 1c$. The second mesh (1.66M nodes), called Mesh2, contains 51 slices with $Lz = 1c$. The third mesh (6.1M nodes), called Mesh3, is made of 201 slices for an increasing wingspan $Lz = 4c$.
Results are presented in Table 4 and Figures 2 and 3.

Name	Mesh size	$\overline{C}_d$	$\overline{C}_l$	St
Present simulations				
DDES $k-\varepsilon$	0.5M	1.65	1.00	0.12
DDES $k-R$	0.5M	1.26	1.05	0.30
DDES SA, mesh-adaptation	0.2M	1.53	0.97	0.165
URANS $k-\varepsilon$	0.5M	2.12	1.28	0.26
URANS $k-R$	0.5M	2.52	1.55	0.28
URANS/DVMS ($k-\varepsilon$, $f_d = f_{\text{ddes}}$)	0.5M	1.54	0.95	0.30
URANS/DVMS ($k-\varepsilon$, $f_d = f_{\text{geo}}$)	0.5M	1.66	1.03	0.33
URANS/DVMS ($k-R$, $f_d = f_{\text{geo}}$)	0.5M	1.86	1.24	0.20
DDES/DVMS ($k-\varepsilon$, $f_d = f_{\text{ddes}}$)	0.5M	1.64	1.01	0.32
DDES/DVMS ($k-\varepsilon$, $f_d = f_{\text{geo}}$)	0.5M	1.77	1.06	0.33
NOISEtte simulations				
DDES SA, Mesh1	1.15M	1.72	1.03	0.19
DDES SA, Mesh2	1.66M	1.7	1.02	0.2
DDES SA, Mesh3	6.1M	1.49	0.91	0.2
Other simulation				
DES/OES $k-\omega$, $Lz = 4c$ [7]	2M	1.682	1.000	0.186
Experiment [13]		1.517	0.931	.17 and .34

Table 1: NACA0021 benchmark: bulk coefficients. $\overline{C}_d$ and $\overline{C}_l$ hold for the mean drag and lift coefficients, and St for the Strouhal number.

First of all, we can note that the RANS results are the least satisfactory with largely overestimated bulk coefficients. This observation is not very surprising, these models being moderately efficient in the case of massively separated unsteady flows. Regarding the results obtained with the AIRONUM software, we observe also that the hybrid results show a good overall agreement with the experimental data, the best results being obtained by the hybrid strategy which combines the RANS $k-\varepsilon$ model of Goldberg with the DVMS approach and with the choice of the shielding function $f_d = f_{\text{ddes}}$. It can be noted that DDES with mesh adaptation computed by NiceFlow software also gives good bulk coefficients, and that the agreement is less satisfactory when the RANS $k-R$ model is used in the hybrid computations compared to the counterpart approaches based on the RANS $k-\varepsilon$ model.
As for the results obtained with the NOISEtte software and meshes Mesh1, Mesh2 and Mesh3, one can notice a good agreement with the hybrid results calculated with the AIRONUM software. It can also be noticed from Table 4 and Figure 3 that the results are improved when more

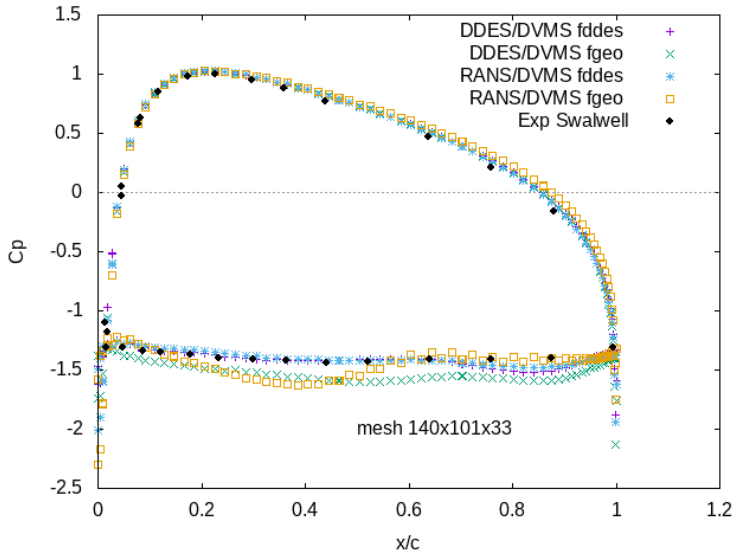

Figure 2: NACA0021 benchmark: distribution of the mean pressure coefficient over the airfoil for the 3D fixed mesh (hybrid calculations using the RANS $k-\varepsilon$ model of Goldberg and AIRONUM CFD software).

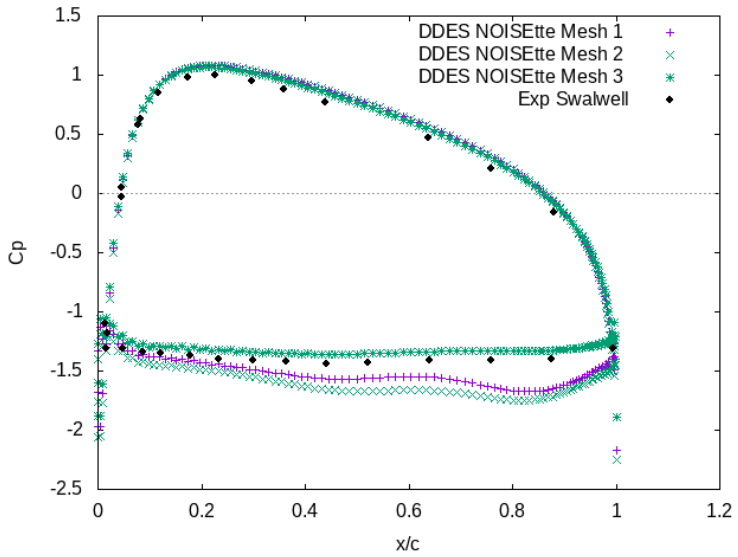

Figure 3: NACA0021 benchmark: distribution of the mean pressure coefficient over the airfoil for meshes Mesh1, Mesh2 and Mesh3 using the Spalart-Allmaras DDES model and NOISEtte software.

slices are used in the transverse direction and the wing span is increased (Mesh3).

5 FLOW PAST A CARADONNA-TUNG HELIX

5.1 Experimental setup

The CFD results are compared against the experimental data obtained by Caradonna and Tung [5]. This test-case is extensively used within the helicopter community for validation of CFD codes applied to rotorcraft problems. The rotor model consists of two rectangular, untwisted and untapered rigid blades mounted on a tall column containing a drive shaft located in a large chamber with special ducting designed to eliminate room recirculation. Each blade shape is based on the NACA0012 airfoil. The chord length is 0.1905 m and rotor radius is 1.143 m. In our computations the rotation speed is 650 RPM. The pressure distributions have been measured at five cross-sections of the blade and the tip vortex trajectory has been extracted using a hotwire technique.

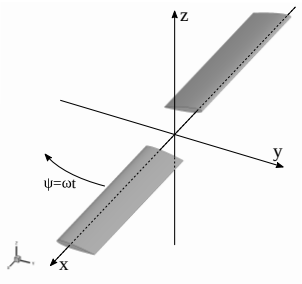

Figure 4: Caradonna-Tung rotor numerical setup.

5.2 Numerical conditions

The Reynolds number based on the blade chord b, tip velocity V_{tip}, air density $\rho_0 = 1.239\ kg/m^3$ and dynamics molecular viscosity $\mu_0 = 1.822 \times 10^{-5}\ H \cdot s/m^2$ corresponding to the air temperature $16^\circ\ C$, is given by $Re = 1.01 \times 10^6$. The computational domain is a cylinder, whose axis coincides with the axis of rotation of the rotor. The computational domain is discretized with an unstructured mixed-element mesh that is refined in the regions requiring a detailed prediction of aerodynamic effects. Thus, the most detailed mesh is built on the rotor blade surfaces, near the leading and trailing edges and near the blade tip. Within the computational domain, starting from the rotor surface the layers of the prismatic mesh are constructed with exponentially increasing heights. Moving away from solid surfaces and as prisms of isotropic dimensions are reached, the volume mesh becomes tetrahedral, the tetrahedron heights increasing with distance from the rotor. The mesh generated by the POINTWISE software for the RANS-based simulation contains 3.4M vertices. The mesh build for the scale-resolving simulation with NOISETTE contains 150M vertices.

A preliminary computation was also performed with the mesh adaptive code, the V6 approximation and the SA model, using 2.2M vertices.

5.3 Numerical results

Figure 5, 6 represent the pressure coefficient distribution along the blade at specific section locations. It can be observed a good agreement with experimental data and, as it is expected, the RANS and DES calculations give almost the same near-blade flow properties and pressure distribution along the blade.

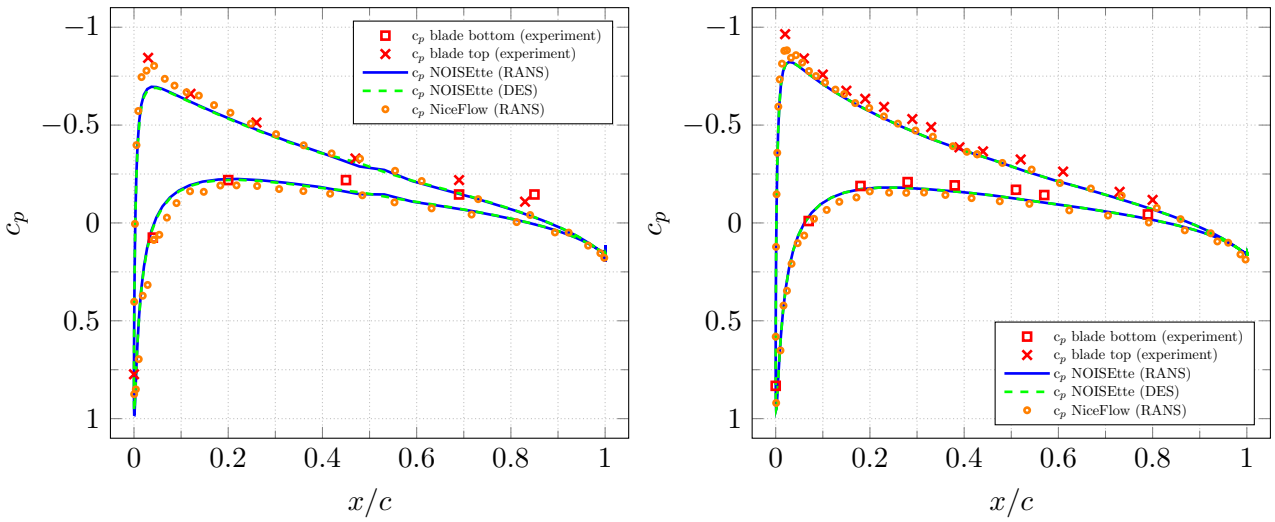

Figure 5: Pressure coefficient at $r/R = 0.5$ (left) and $r/R = 0.68$ (right) blade sections.

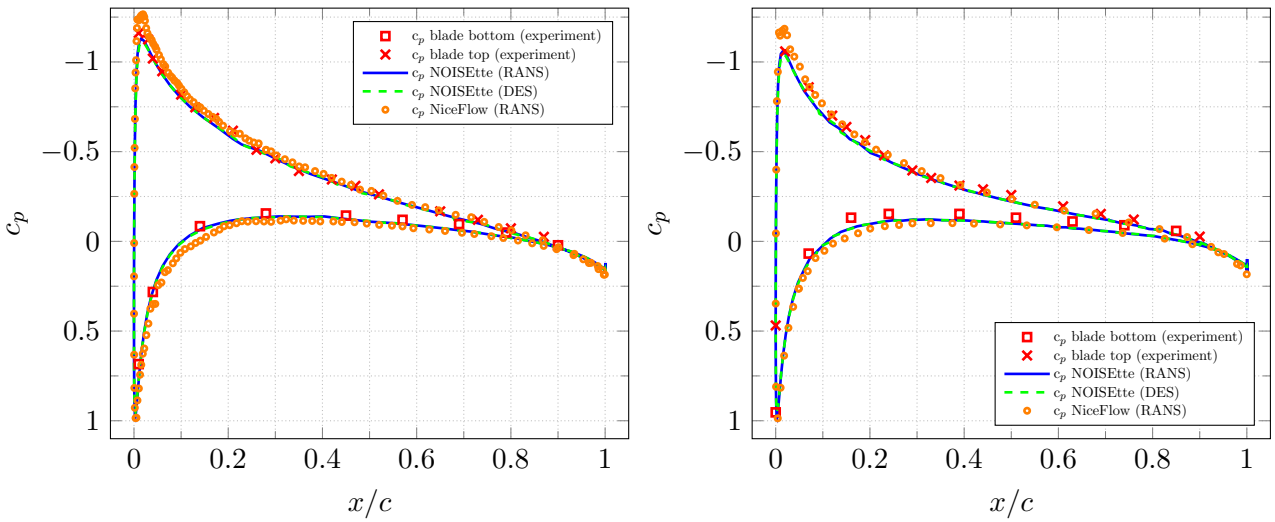

Figure 6: Pressure coefficient at $r/R = 0.89$ (left) and $r/R = 0.96$ (right) blade sections.

In Figure 7, the tip vortex position is compared against experimental data and analytical model prediction [9]. As for the wake descent (z/R), both computational results are close to the

experiment and predicted tip vortex position for the whole observed vortex age. The tip vortex contraction (r/R) predicted in RANS and DES calculations are well aligned with experimental data for vortex age up to 200°. The discrepancy increases with wake age increase, however the DES prediction is a bit closer to the experimental data.

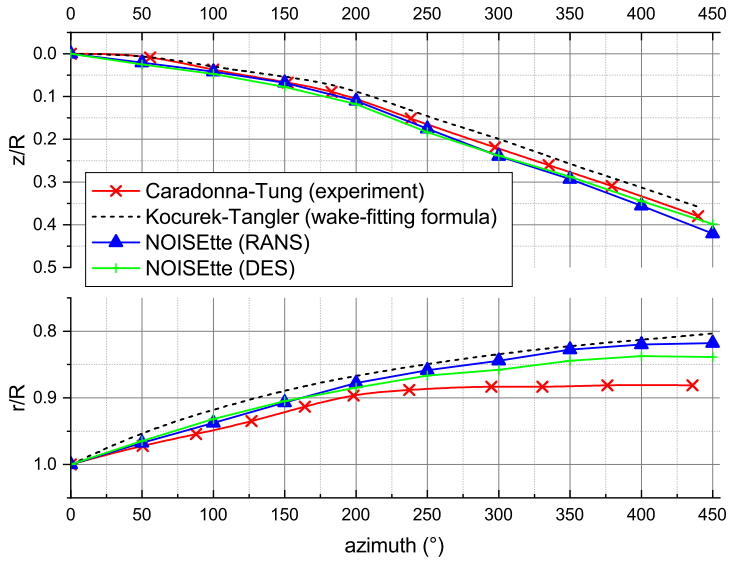

Figure 7: Tip vortex position.

6 CONCLUDING REMARKS

The low-dissipation methods used in this work allow computations with rather coarse meshes, and in particular very coarse adapted meshes. They are still of low computational cost per vertex, alllowing the use of much finer meshes. Two test cases are considered with the purpose of predicting noise emission in rotating devices. The NACA0021 at high angle of attack is used to analyse the positive impact of hybridization between RANS-like modeling and LES-like ones. Mesh adaptation could be applied with a reasonable accuracy. The Caradonna-Tung helix is also computed. The fixed mesh calculations match experiments well. The mesh adaptative approach needs further improvements which will be discussed during the talk.

REFERENCES

[1] Abalakin I. and Bakhvalov P. and Kozubskaya, T., Edge-based reconstruction schemes for unstructured tetrahedral meshes, *International Journal for Numerical Methods in Fluids*, 1097-0363, 81, 6, 331–356, 2016, DOI10.1002/fld.4187.

[2] Alauzet, F., Frey, P.J., George, P.-L., and Mohammadi, B.. 3D transient fixed point mesh adaptation for time-dependent problems: Application to CFD simulations. *J. Comp. Phys.*, 222:592–623, 2007.

[3] Bakhvalov, P. A. and Kozubskaya, T. K., Construction of edge-based 1-exact schemes for solving the Euler equations on hybrid structured meshes, 57, 4, *Computational Mathematics and Mathematical Physics*, Pleiades Publishing Ltd, 2017, 4, 680697, url-http://dx.doi.org/10.1134/S0965542517040030.

[4] Camarri, S., Koobus, B., Salvetti, M. V., and Dervieux, A. A low-diffusion MUSCL scheme for LES on unstructured grids. *Computers and Fluids*, 33:1101–1129, 2004.

[5] Caradonna, F. X. and Tung, C. Experimental and analytical studies of a model helicopter rotor in hover. *NASA-TM-81232*, NASA, Ames Research Center, Moffett Field, California, 9, 1981.

[6] Debiez, C. and Dervieux, A. Mixed element volume MUSCL methods with weak viscosity for steady and unsteady flow calculation. *Computer and Fluids*, 29:89–118, 1999.

[7] El Akroury, R., Braza, M., Hoareau, Y., Vos, J., Harran, G. and Sevrian, A. Unsteady Flow Around aNACA0021 Airfoil Beyond Stall at 60 deg. angle of attack. IUTAM Symposium on Unsteady Separated Flows and their Control, pp 405-415, 2021.

[8] Goldberg, U., Peroomian, O., Chakravarthy, S., 1998, A wall-distance-free $k-\varepsilon$ model with Enhanced Near-Wall Treatment, *Journal of Fluids Engineering*, Vol. 120, pp. 457–462.

[9] Kocurek, J. David, Tangler, James L.. A Prescribed Wake Lifting Surface Hover Performance Analysis. *Journal of the American Helicopter Society*, American Helicopter Society, 22, 1, 1977, 1, 2435, url=http://dx.doi.org/10.4050/JAHS.22.24, DOI10.4050/jahs.22.24.

[10] Moussaed, C., Wornom, S., Salvetti, M., Koobus, B., Dervieux, A. Impact of dynamic subgrid-scale modeling in variational multiscale large-eddy simulation of bluff body flows. *Acta Mechanica* **12**, 3309–3323 (2014)

[11] Spalart, P.R., Allmaras, S.R. A one-equation turbulence model for aerodynamic flows. In *30th AIAA Aerospace Sciences Meeting and Exhibit*, AIAA-92-0439, Reno, NV, USA, Jan 1992.

[12] Swalwell, K.E., Sheridan, J., Melbourne, W.H. Frequency Analysis of Surface Pressures on an Airfoil After Stall. 21st AIAA Applied Aerodynamics Conference. Orlando, FL, USA. American Institute of Aeronautics and Astronautics, June 2003.

[13] Swalwell, K.E. The effect of turbulence on stall of horizontal axis wind turbines. PhD, Monach University, Australia (2005).

[14] Yang Zhang, Md Mizanur Rahman, Gang Chen. Development of k-r turbulence model for wall-bounded flows. *Aerospace Science and Technology*, 98:105681, 2020.